ACS Catalysis

Research Article

pubs.acs.org/acscatalysis

Improved Oxygen Reduction Activity and Durability of Dealloyed $PtCo_x$ Catalysts for Proton Exchange Membrane Fuel Cells: Strain, Ligand, and Particle Size Effects

Qingying Jia,[†] Keegan Caldwell,[‡] Kara Strickland,[†] Joseph M. Ziegelbauer,[§] Zhongyi Liu,[§] Zhiqiang Yu,[§] David E. Ramaker,[‡] and Sanjeev Mukerjee*[,†]

[†]Department of Chemistry and Chemical Biology, Northeastern University, Boston, Massachusetts 02115, United States

[‡]Department of Chemistry, George Washington University, Washington, DC 20052, United States

[§]Electrochemical Energy Research Lab, General Motors Central Research and Development, Warren, Michigan 48090, United States

Supporting Information

ABSTRACT: The development of active and durable catalysts with reduced platinum content is essential for fuel cell commercialization. Herein we report that the dealloyed PtCo/HSC and $PtCo_3$/HSC nanoparticle (NP) catalysts exhibit the same levels of enhancement in oxygen reduction activity (~4-fold) and durability over pure Pt/C NPs. Surprisingly, ex situ high-angle annular dark field scanning transmission electron microscopy (HAADF STEM) shows that the bulk morphologies of the two catalysts are distinctly different: D-PtCo/HSC catalyst is dominated by NPs with solid Pt shells surrounding a single ordered PtCo core; however, the D-$PtCo_3$/HSC catalyst is dominated by NPs with porous Pt shells surrounding multiple disordered PtCo cores with local concentration of Co. In situ X-ray absorption spectroscopy (XAS) reveals that these two catalysts possess similar Pt−Pt and Pt−Co bond distances and Pt coordination numbers (CNs), despite their dissimilar morphologies. The similar activity of the two catalysts is thus ascribed to their comparable strain, ligand, and particle size effects. Ex situ XAS performed on D-$PtCo_3$/HSC under different voltage cycling stage shows that the continuous dissolution of Co leaves behind the NPs with a Pt-like structure after 30k cycles. The attenuated strain and/or ligand effects caused by Co dissolution are presumably counterbalanced by the particle size effects with particle growth, which likely accounts for the constant specific activity of the catalysts along with voltage cycling.

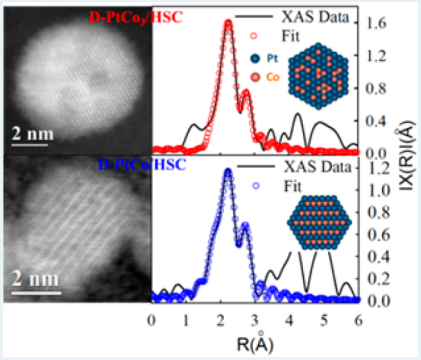

KEYWORDS: *Pt-based nanocatalysts, ORR, in situ XAS, strain effects, ligand effects, particle size effects*

1. INTRODUCTION

Proton exchange membrane fuel cells (PEMFCs) have been considered ideal power sources due to their high energy efficiency, high power density, and low emissions.[1−3] For PEMFCs, the sluggish kinetics of the oxygen reduction reaction (ORR) at the cathode is the key challenge for the commercial viability, especially for transportation applications. Pt-based catalysts are the practical materials in terms of both activity and durability so far, although the iron-based catalysts recently developed by Dodelet et al.[4] exhibit ORR activity approaching that of commercial Pt/C catalysts in acidic environments. However, the limited availability and high cost of platinum severely hampers successful fuel cell commercialization. To address this problem, Pt-based bimetallic nanocatalysts (PtM: the M is usually the transition element such as Fe, Co, Ni, etc.) have been extensively investigated for use as cathode catalysts in PEMFCs with the aim of improving the ORR activity and providing some cost reduction by decreasing the Pt loadings.[5−11] Pt-mass-based activity (MA) enhancement of a factor of 1.5−2.5 compared to pure Pt has been reported in conventional PtM nanoparticles (NPs).[12−17] Recently, dealloyed PtM NP alloys developed by Strasser et al.[18−20] exhibit approximately 4−8 times higher MA and 4−7 times higher Pt electrochemical surface area (ECSA)-based specific activities (SA) for ORR than the state-of-the-art Pt/HSC. Durability studies of these catalysts reveal superior MA after long-term operation in PEMFCs compared to commercial pure Pt.[20,21] Moreover, the distinct core−shell structure of these dealloyed catalysts makes it possible to have some synthetic control of the metal shell activity through interactions with the core.

Significant research efforts have been focused on elucidating the origin of the enhanced ORR activity of Pt-based alloys relative to pure Pt.[16,22−28] Great progress has been made by the collaborative efforts between Stamenkovic's group (experimental work)[24,29] with Nørskov's groups (theoretical calculations).[16,23,30,31] They demonstrate that the enhanced ORR activity of $Pt_3M(111)$ can be attributed to the weakening Pt−O bond strength relative to Pt(111), which is due to the downshift of Pt *d-band* center (ε_d) relative to the Fermi level.

Received: June 26, 2014
Published: November 19, 2014

In addition, ε_d is shown to be directly correlated to ORR kinetics with a general consensus of a volcano type behavior based on choice of alloying element. Today, ε_d has been generally accepted as a valid descriptor of the ORR activity of PtM alloys[32−34] with some limitations.[35]

It has been postulated that the ORR mechanism established for extended Pt alloy surfaces can be applied to understand the activity of supported PtM NPs.[29,36] However, the efforts of using the d-band center as a ORR activity descriptor for PtM NPs have been stymied by the fact that it can only be measured on well-defined surfaces under ultrahigh vacuum (UHV), whereas the surface composition and morphology of PtM NPs often change drastically in the electrochemical environment during reactions. Alternatively, extensive research has focused on characterizing the atomic-scale structure and electronic property of PtM NPs,[25,28,34,36−39] which are correlated to the d-band center and then linked to their ORR activities based on the strain, ligand, and particle size effects established on well-defined models.[26,30,40]

Equation 1 developed by Nørskov et al.[40] has been used to describe the ligand and strain effects:

$$V_i = 7.62 \sum_{j=1}^{CN} \frac{[r_d^{(i)} r_d^{(j)}]^{3/2}}{d_{ij}^{5}} \quad (1)$$

where V_i is the interatomic matrix element that describes interaction between an atom and its environment, and is proportional to the d-band width according to tight binding theory. Because the root mean squared (rms) d-band width is inversely proportional to the d-band center,[40] V_i is monotonically related to d-band center ε_d. $r_d^{(i)}$ is a characteristic radius that is related to the spatial extent of the *d-orbitals* of that metal *i*; CN is the number of the nearest neighbors (first-shell coordination number); and d_{ij} is the bond distance between adjacent atoms *i* and *j*. Strain effects are incorporated into the denominator through d_{ij}, Thus, shortening the d_{ij} results in the broadening of the d-orbital and downshift of d-band center and thereby reduces the binding energies of simple adsorbates such as O, H, and OH. Strain has long been recognized as a key determinant of ORR activity in Pt alloys that generally possess altered d_{ij}(s) compared to pure Pt.[14,41] Recently, Strasser et al.[25] attributed a 6-fold enhancement in ORR activity of dealloyed $PtCu_x$ over pure Pt NPs to the isolated strain effects, given the fact that the thickness of the pure Pt overlayer (∼1 nm) in dealloyed $PtCu_x$ exceeds the effective range of ligand effects.

Ligand effects are incorporated into the numerator of eq 1 through the $r_d^{(i)}$ of each metal, as well as the denominator through d_{ij}. Unlike strain effects, the role of ligand effects in ORR activity of PtM NPs has been elusive. For example, Chen et al.[36] observed a "sandwich-segregation" structure for the heat-treated "Pt_3Co" NPs using ex situ STEM, and they attributed the high ORR specific activity (SA) to the cooperative strain and ligand effects induced by the abundant subsurface Co. Similarly, Chunhua et al.[38] reported that among three octahedral Pt_xNi_{1-x} catalysts Pt_1Ni_1 exhibited the highest ORR activity, which was attributed to the additional ligand effects brought by the enriched subsurface Ni in the Pt_1Ni_1 catalyst. On the contrary, Xin et al.[42] stated that the subsurface Co of the heat-treated Pt_3Co NPs cannot survive exposure to acid and that the catalytic enhancement should be ascribed to strain effects instead of the nearest neighbor ligand effects. Likewise, the exceptional ORR activity of a new class of Pt−Co NPs composed of ordered Pt_3Co cores with a 2−3 atomic layers of platinum developed by Wang et al.[43] was attributed to strain effects, and the ligand effects were excluded due to the lack of subsurface Co. The different views of the role of ligand effects could arise from either the different (near)surface structure and composition of various PtM NP catalysts, and/or the limitations of ex situ characterization techniques because the morphology and (near)surface composition often changes during electrochemical potential cycling.[37,38]

Particle size is another key determinant of ORR activity in Pt-based NPs.[44−49] The ORR specific activity (SA) of PtM NPs generally decreases with decreasing particle size, especially when the particle size is smaller than 5 nm.[44,47] It has been shown[50,51] that the dependence of catalytic activity on cluster size correlates well with the coordination number: smaller particles have more under-coordinated atoms in the kinks, edges, steps, or more open surfaces such as (110) and (100). According to eq 1, these under-coordinated atoms have higher d-band centers than the close-packed surfaces (such as (111) or hex reconstructed (100)) and thus are more prone to be poisoned by intermediate oxygenated species due to the stronger binding energy. It is worthwhile to mention that Han et al.[52] reported that although the d-band center theory captures the overall tendencies of chemical reactivity as a function of particle size, it does not capture most of the variation between different sites and particle size. In addition, Yu et al.[35] recently showed that the d-band center is poorly related to the Pt−O binding energy and thus the ORR activity when comparing the same metal with different surface plane orientations. Therefore, the particle size effects may not be fully accounted for by d-band center theory.

Strain, ligand, and particle size effects also play important roles in determining the durability of Pt-based catalysts. The durability of pure Pt/C NPs is primarily governed by the particle size effects. Specifically, as the pure Pt/C NPs grow with voltage cycling, the SA increases up to three- to 4-fold, which is compensated for by a drastic loss of ECSA up to ∼75%.[21,31,53−55] As a result, the mass activity (MA) of pure Pt/C generally drops with voltage cycling. On the other hand, strain, ligand, and particle size effects often coimpact the durability of PtM NPs, as the voltage cycling results in not only the particle growth[21,56] but also the dissolution of the soluble metal M that leads to the increase in the Pt-enriched outer layer thickness.[57] The SA of PtM NPs governed by the particle size effects is expected to increase with voltage cycling as occurred on pure Pt/C NPs, whereas the SA governed by the strain and ligand effects decreases with M loss.[57] The overall specific activity trend of PtM with voltage cycling depends upon which effects dominates and this can account for the different SA trends observed with voltage cycling on various PtM NPs.[21,53−55,58] The MA of PtM catalysts generally drops with long time operation but still maintains a ∼2-fold gain compared with aged Pt catalysts.[34,53,54] However, the origin of the enhanced durability of PtM catalysts over Pt/C catalysts is still unclear because the convoluted strain, ligand, and particle size effects in PtM catalysts significantly complicates the structure/activity correlations.

Besides strain, ligand, and particle size effects, other factors such as the lateral repulsive interaction between like adsorbates,[59,60] the alloying extent,[61] and so on may also affect the catalytic activity of Pt-based catalysts. The improved ORR activity and durability of PtM NPs often represents the sum of contributions from more than one effect depending on the

dx.doi.org/10.1021/cs501537n | ACS Catal. 2015, 5, 176−186

morphology and composition. In this regard, in situ XAS offers a unique opportunity to provide a comprehensive understanding of the PtM NPs catalysis by quantitatively determining the bond distance d_{ij}, the specific element M ($r_d^{(i)}$), and the coordination number CN under in situ operating conditions that are directly related of strain, ligand, and particle size effects, respectively.[26] In addition, the $\Delta\mu$ technique developed by Ramaker et al.[62−65] has evolved into a powerful tool for elucidating surface adsorbed species, surface structure, and composition in electrocatalysis and hereby extends the XAS from a bulk-averaging structural technique into a surface sensitive technique.

In this context, we report that the dealloyed PtCo/HSC and $PtCo_3$/HSC NPs exhibit the same levels of enhancement in ORR activity and durability relative to Pt/C NPs despite their dissimilar morphologies as revealed by ex situ HAADF STEM. In situ XAS analysis was performed on these two catalysts to identify whether the morphologies of the catalysts in the in situ electrodes changes substantially under reactive conditions as compared to dry powders. Several quantities that have been previously related to PtM ORR activity such as the Pt d-band vacancy, the atomic distribution, the Pt−Pt and Pt−Co bond distances, and the Pt coordination numbers are obtained by combined X-ray absorption near edge analysis (XANES) and extended X-ray absorption fine structure (EXAFS) analysis. Their implications to the intrinsic ORR activity of the catalysts are systemically discussed. In addition, the evolution of the morphology of dealloyed $PtCo_3$/HSC NPs with voltage cycling is studied by performing ex situ XAS on the catalyst under different voltage cycling stages to understand the decline of the activity with the voltage cycling.

2. EXPERIMENTAL SECTION

2.1. Catalyst Preparation. The dealloyed $PtCo_3$/HSC and PtCo/HSC were produced by via a three step process: (1) the precursor was prepared by an impregnation method, (2) followed by a high-temperature annealing step, and (3) chemically dealloyed by acid leaching. A commercial Pt/high-surface carbon (HSC) powder (Tanaka Kikinzoku Kogyo (TKK), Japan, 28.1 wt % Pt) was impregnated with an aqueous solution of cobalt chloride (concentration: 0.4 M) to give a Pt/Co atomic ratio of 1:3 or 1:1 and dried at 80 °C for 24 h. The resultant precursor was then annealed at 900 °C in 10 vol % H_2/N_2 for 5 h to sufficiently reduce the Co and interdiffuse it with the Pt to form Pt−Co alloy nanoparticles. The 900 °C annealing temperature was chosen here also because dealloyed PtM catalysts annealed in the range of 800−950 °C show the best ORR performance as they present the most favorable balance between mass, specific ORR activity, and durability.[18−21,25,66,67] The chemical dealloying was accomplished in a 1 M nitric acid solution at 80 °C for 24 h. Following the dealloying step, the catalyst was filtered with copious amounts of deionized water (18.2 MΩ) and further dried at 80 °C for 24 h. The postdealloying Pt/Co composition of D-$PtCo_3$/HSC and D-$PtCo_1$/HSC catalyst as quantified by inductively coupled plasma (ICP) is 2.7 and 2.2, respectively. The final catalyst powder was then manually ground in an agate mortar and pestle prior to preparing the MEA inks.

2.2. Cell Assembly and MEA Tests. The MEA cathodes were fabricated with the catalyst-coated-membrane (CCM) method via draw down with a Meyer rod and then decal transfer. The catalyst solution comprised the catalyst powder, Nafion ionomer (925 EW), Pt loading of 0.2 mg_{Pt} cm^{-2}. The anode electrode had a Pt loading of 0.05 $mg_{Pt}\cdot cm^{-2}$ and I/C ratio of 0.6. The 50 cm^2 die-cut cathode- and anode-catalyst-coated decals were then hot pressed onto a 25 μm Nafion-111 membrane (NRE211, 1100 EW, EW = $g_{polymer}$ mol^{-1}_{H+}, Dupont) at 140 °C. A proprietary microporous carbon paper layer served as the gas diffusion media (GDM), and "dog-bone" flowfields emulating flow conditions in full-active-area fuel cell stacks were employed. The above-prepared 50 cm^2 MEAs were tested for their cathode ORR kinetic activities under H_2/O_2 (anode/cathode). The H_2/O_2 stoichiometries for the anode and cathode were 2.0 and 9.5, respectively. The relative humidity was maintained at 100%, and the cell total pressure was maintained at 150 kPa_{abs}. Each MEA was subjected to a proprietary break-in procedure in order to fully condition the components of the MEA. Following the break-in, galvanic polarization curves were measured at 0.02, 0.03, 0.05, 0.1, 0.2, and 0.4 A cm^{-2} while holding for 4−6 min at each point. The stabilized cell voltage was averaged over the final minute. The catalytic activity of the cathode catalysts were evaluated at a high frequency resistance (HFR)-corrected voltage of 0.9 V vs RHE at 80 °C. In voltage cycling tests, 200 sccm H_2 (anode) and 50 sccm N_2 (cathode) were admitted at 150 kPa_{abs}. The cell voltage was swept at 50 $mV\cdot s^{-1}$ between 0.05 and 1.0 $V_{(RHE)}$ in a triangle profile. The electrochemical surface areas (ECSAs) of the cathode catalysts were obtained from hydrogen-adsorption/desorption (HAD) analysis by integrating the hydrogen adsorption area over a range of 0.08 to 0.4 $V_{(RHE)}$.

2.3. Electrode Preparation and XAS Data Collection. The electrode inks for the EXAFS electrodes were composed of 1:1 (wt %) 18.2 MΩ purity deionized water (Millipore) and 2-propanol (HPLC-grade, Aldrich), a 5 wt % Nafion solution (Aldrich), and the catalyst powder. The composition was chosen to give a final electrode with a dry Nafion loading of 5 wt %. The ink was hand-painted onto a Zoltek carbon cloth and dried for 15 min in a 65 °C vacuum oven between coats. The final Pt and Co geometric loadings were chosen to give 0.1 edge heights at the Pt L_3 and Co K edges, respectively. XAS experiments were performed on D-PtCo/HSC [Advanced Photon Source (beamline XOR-9BM) in Argonne National Laboratory] and D- $PtCo_3$/HSC [X3B beamline of National Synchrotron Light Source (NSLS, Brookhaven National Laboratory, NY)] at room temperature in an in situ specially designed electrochemical XAS half cell. The cell was flooded with N_2 or O_2-saturated 0.1 M $HClO_4$ electrolyte during operation. Full range Pt $L_{2,3}$ and Co K spectra were taken at various static potentials along the anodic sweep of the cyclic voltammetry (CV). Data were collected in fluorescence mode with a Pt/Co reference foil positioned between I2 and I3 as a reference. The voltage cycling limits were 0.05 to 1.10 V versus RHE. Data collection was performed at the chosen potentials held during anodic sweeps. The electrode was fully cycled following each potential hold in order to clean the electrocatalyst surfaces after each potential hold. In addition to in situ data collection on fresh samples, ex situ measurements were performed on aged D-$PtCo_3$ single-sided MEAs (0−30k voltage cycles between 0.6−1.0 V vs RHE in PEMFCs).

2.4. High-Angle Annular Dark Field Scanning Transmission Electron Microscopy (HAADF STEM). HAADF STEM imaging was performed on D-$PtCo_3$/HSC and D-PtCo/HSC NPs with an aberration-corrected JEOL JEM-2100F microscope in a scanning transmission electron microscopy (STEM) mode operated at 200 kV. Samples suitable for the

dx.doi.org/10.1021/cs501537n | ACS Catal. 2015, 5, 176−186

HAADF imaging were prepared by grinding the as-synthesized powder between two clean glass slides and then dusting the ground fine powder onto lacy-carbon-coated Cu TEM grids.

2.5. XAS Data Analysis. The data were processed and fitted using the Ifeffit-based Athena[68] and Artemis[69] programs. Scans were calibrated, aligned, and normalized with background removed using the IFEFFIT suite[70] (version 1.2.9, IFEFFIT Copyright 2005, Matthew Newville, University of Chicago, http://cars9.uchicago.edu/ifeffit/). The $\chi(R)$ were modeled using single scattering paths calculated by FEFF6.[71]

3. RESULTS AND DISCUSSION

3.1. Electrochemical Characterization. The ORR activities and ECSAs of the D-PtCo$_3$/HSC and D-PtCo/HSC, tested in a 50 cm^2 geometric-area MEA (0.2 mg$_{Pt}$·cm^{-2} loading) in O_2/H_2 are shown in Figure 1.[73] The Pt-based mass

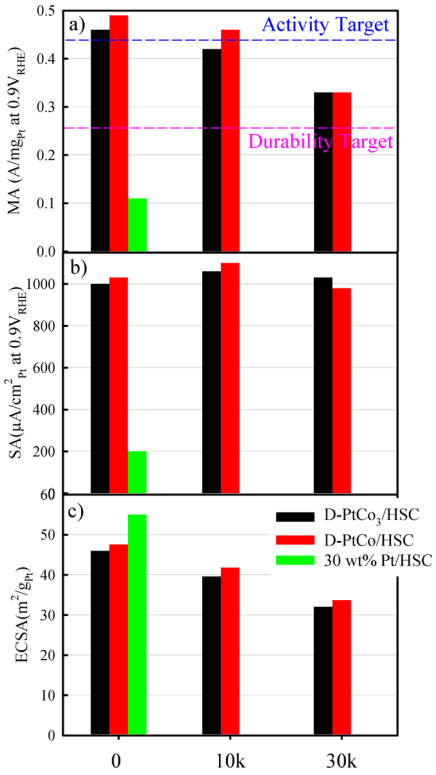

Figure 1. (a) Mass activity, (b) specific activity, and (c) electrochemical surface area (ECSA) of dealloyed PtCo$_3$/HSC (in black) and PtCo/HSC (in red) catalysts during the voltage cycling tests of MEAs. Conditions: 80 °C, 100% RH, 50 sccm H_2 in anode, 200 sccm N_2 in cathode, voltage range of 0.6−1.0 V (vs RHE), and scan rate at 50 mV·s^{-1}. The results of fresh 30 wt % Pt/HSC (in green) obtained in the same conditions are included for comparison. The 2017 DOE (Department of Energy) target[72] of mass activity and durability are indicated as blue and pink dashed lines, respectively.

activity (MA) at 0.9 V vs RHE of the fresh (0k) D-PtCo$_3$/HSC and D-PtCo/HSC is 0.46 and 0.49 A·mg$_{Pt}^{-1}$, respectively, both exceeding the 2017 DOE target of 0.44 A·mg$_{Pt}^{-1}$.[72] After voltage cycling (30k cycles at 0.6−1.0 V vs RHE), the MA of both samples decreases to 0.33 A·mg$_{Pt}^{-1}$ (~34% decline), exceeding the 2017 DOE target of 0.26 A·mg$_{Pt}^{-1}$ as well.[72] The MA(s) and SA(s) of both fresh catalysts are ~4 and ~5 times higher than that of the state-of-the-art Pt/HSC NPs, respectively. The drop of the MA(s) for both catalysts with voltage cycling is primarily ascribed to the reduction of the ECSA(s) (Figure 1c) as the SA(s) maintain nearly constant (Figure 1b). The MA, SA, and ECSA of the two catalysts are very close, which insinuates that the two catalysts possess similar structural and electronic properties. To test this hypothesis, ex situ HAADF STEM in conjunction with in situ XAS are utilized to characterize the structure of the catalysts on the atomic scale.

3.2. HAADF STEM Imaging. HAADF-STEM images (Figure 2) show that the D-PtCo/HSC is dominated

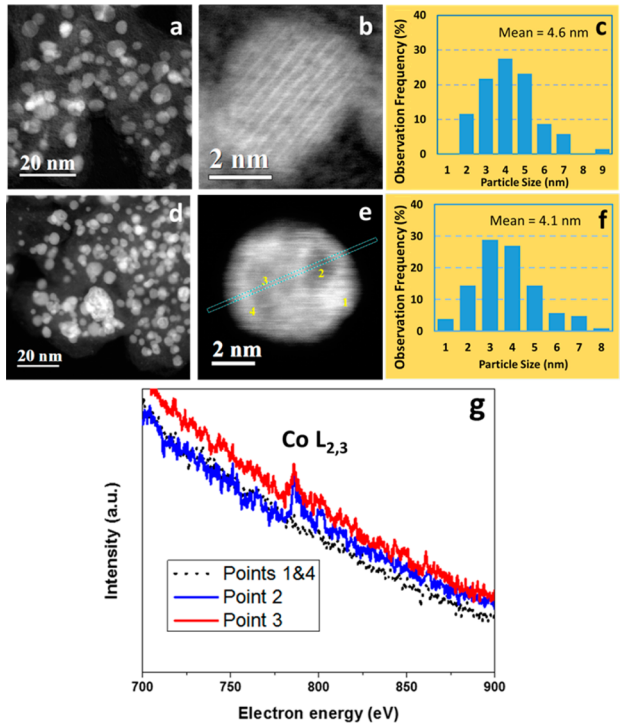

Figure 2. (a−c, upper panel): HAADF images at low and high magnifications showing D-PtCo/HSC NPs and their particle size distribution; (d−f, lower panel): HAADF images at low and high magnifications showing D-PtCo$_3$/HSC NPs and their particle size distribution; (g): EELS spectra taken from points 1−4 in the HADDF image e).

(~90%) by particles with an alternating arrangement of individual columns of atoms of different intensities (Figure 2b). The ADF image contrast is a function of mass (or thickness) and atomic number Z (proportional to Z$^{\sim 1.7}$). The contrast of the Pt atoms is about 6 times higher than that of the Co atoms. For a small Pt−Co NP (3−5 nm), the difference in the thickness from the particle center to the outer region is very small, thus negligible. Therefore, the alternating intensities reflect the alternating arrangement of Pt and Co atomic planes, evidencing the ordered distribution of Pt and Co atoms in D-PtCo/HSC NPs. A similar structure was reported on ordered "Pt$_3$Co" NPs with "Pt-skin" surfaces, which are obtained by annealing commercial Pt$_3$Co NPs.[42,74] Therefore, these particles are referred to as Pt$_{shell}$/single-PtCo$_{core}$ particles. On the other hand, Figure 2d,e suggest that the majority of the particles in D-PtCo$_3$/HSC have significant intensity variations (dark spots), with several dark spots within each of the particles. EELS (electron energy loss spectroscopy) spectra taken from four different points in a representative particle (Figure 2e,g) indicate pure Pt outer shell (no Co L$_{2,3}$ edges seen at 778 eV for point 1 and 4) and the presence of the Co in

dx.doi.org/10.1021/cs501537n | ACS Catal. 2015, 5, 176−186

the dark-patches (Co $L_{2,3}$ edges clearly seen at 778 eV for point 2 and 3). A more detailed analysis[75,76] of the ADF and EELS-mapping images of D-$PtCo_3$/HSC suggests that the "dark spots" can be either Co-rich regions or real voids, and several different areas of local concentration of Co are often seen within a particle. Therefore, these particles are described as Pt_{shell}/multi-$PtCo_{core}$ particles. Despite their different particle morphology, both catalysts possess comparable mean particle sizes (4.1 and 4.6 nm) with narrow size distributions (Figure 2c,f).

Besides the profound difference in particle morphology between D-PtCo/HSC and D-$PtCo_3$/HSC NPs, their compositional changes during the dealloying process are also quite different. The Co/Pt atomic ratio (1:1) of the D-PtCo/HSC precursor is much lower than that of D-$PtCo_3$/HSC precursor (3:1), whereas the final ratio of D-PtCo/HSC (1:2.2) is higher than that of D-$PtCo_3$/HSC (1:2.7), corresponding to ∼54% and ∼88% loss of Co content, respectively. This indicates that the D-$PtCo_3$/HSC catalyst is subjected to a higher extent of Co dissolution than D-PtCo/HSC during the dealloying process. It was summarized[34] that "the propensity of a Pt-alloy nanoparticle towards solute metal dissolution, or dealloying, is determined by (a) the diffusivity of the solute metal (b) the diffusion length of the solute metal within the nanoparticle (c) the extent of the direct interaction between the subsurface solute metal and adsorbed O* and OH*, and (d) the integrity of the Pt overlayer." It is reasonable to assume that the diffusivity and the diffusion length of Co within D-$PtCo_3$/HSC or D-PtCo/HSC NPs are not significantly different, and the third factor is negligible because both catalysts underwent identical dealloying process in deoxygenated acid. Thus, the lower degree of Co dissolution in D-PtCo/HSC is primarily ascribed to the higher integrity of the Pt overlayer. HAADF-STEM images (Figure 2) indeed show that the D-PtCo/HAS NPs is generally more solid than the D-$PtCo_3$/HAS NPs. These results are in agreement with previous findings[57] that $PtCo_x$ precursor powder with x equal/greater than 1 form skeleton/percolated particles after acid leaching, and the Co concentration is much higher in the skeleton than in the percolated particles. According to the nanoporosity evolution mechanism developed by Erlebacher et al.,[77] the leaching of Co from the surface will leave behind an under-coordinated and hole-rich Pt shell, which is susceptible to surface diffusion and rapidly forms a compact Pt shell. However, if the Co concentration is above the critical value, the etching rate of the Co becomes comparable to the surface diffusion rate of the Pt, and the system is inherently unstable and will spontaneously phase-separate. As a result, the local clustering of Pt leaves the interior Co exposed to the electrolyte, which in turn causes it to be leached away forming a "spongy" structure.[77] Therefore, the precursor composition of D-$PtCo_x$ plays a critical role in determining the postdealloying particle morphology and composition.

Generally, Pt-based NPs with dissimilar atomic structures and compositional distributions exhibit different ORR activity and/or stability.[36,74,78] Here, in spite of the different particle morphology between D-$PtCo_3$/HSC and D-PtCo/HSC catalysts, their activities and stabilities are fairly close (Figure 1). It is important to note that thus far the catalysts have been characterized using ex situ techniques under conditions relevant to PEMFC operation. Therefore, it is necessary to identify whether the morphology of the catalysts changes drastically when exposed to the electrochemical environment under reaction conditions. To address this question, in situ spectroscopic characterization of these catalysts was conducted under working conditions.

3.3. In Situ XAS. *3.3.1. In Situ XANES.* Figure 3a presents the Co K-edge XANES signal of D-$PtCo_3$/HSC and D-PtCo/HSC at 0.54 and 0.90 V together with the Co reference foil for comparison. The corresponding raw $k^2\chi(k)$ XAS data are shown in Figure S1. The formation of a Pt−Co alloy can be identified from the four different features, labeled as A, B, C, and D.[79−81] Compared to the Co foil, features C and D are shifted to lower energies in the PtCo alloy samples due to the expansion of the Co−M bond distances, indicating that Co is involved in a bimetallic phase and alloying with Pt possessing a larger atomic radius.[80,82] In addition, features A and B, respectively, are assigned to electron excitations from 1s to the unoccupied 3d, 4s, and 4p hybridized states. Thus, the decrease of feature A and increase of feature B, both of which vary strongly upon alloying, reflects population rearrangement between the levels involved in these transitions.[80] The A−D features overall suggest that the majority of Co atoms in the sample exist predominantly in a metallic state, albeit with significant modification of its electronic properties from the Pt−Co interactions.

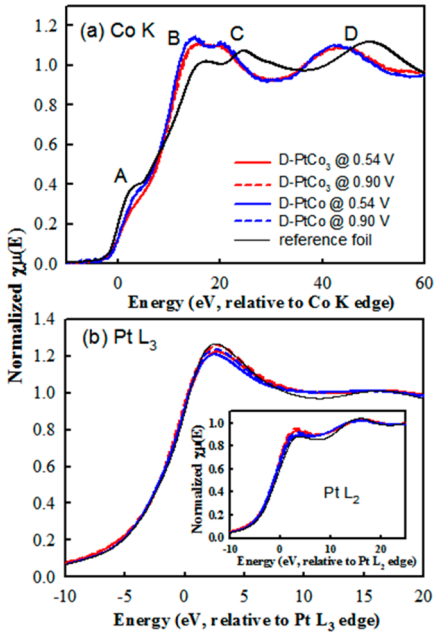

Figure 3. XANES spectra of D-$PtCo_3$/HSC (red), D-PtCo/HSC NPs (blue) at 0.54 and 0.90 V vs RHE, and the corresponding reference foil (black) at Co K edge (a) and at Pt $L_{2,3}$ edges (b).

As shown in Figure 3b, the Pt $L_{2,3}$ XANES of D-$PtCo_3$/HSC and D-PtCo/HSC collected at 0.54 V (double layer region) and 0.90 V in N_2-saturated electrolyte have features that very closely resemble those of Pt foil (black line), indicating the predominantly metallic state of Pt in the samples. The unoccupied Pt d-orbital (e.g., d-band vacancy h_{Ts}) is quantitatively determined from the Pt $L_{2,3}$ XANES following the method developed by Mansour et al.[83] As listed in Table 1, both catalysts exhibit lower h_{Ts} than that of Pt/C with particle size ranging from 3 to 9 nm.[45] On the contrary, Mukerjee et al.[13,14] reported that conventional Pt_3Co/C alloys (averaged particle size: 5.6 nm (ETEK); 6.9 nm (JMRC)) with less enhanced ORR activity possesses higher h_{Ts} compared to Pt/C.

dx.doi.org/10.1021/cs501537n | ACS Catal. 2015, 5, 176−186

Table 1. Summary of Pt d-Band Vacancy for Pt/C and Various Pt_nCo_m/C NPs at 0.54 V vs RHE

	D-PtCo	D-$PtCo_3$	Pt[a]	Pt_3Co(ETEK)[a]	Pt_3Co(JM)[a]
h_{Ts}	0.31	0.32	0.33	0.37	0.40

[a]Experimental results are collected from ref 13.

These results suggest that the atomic composition plays a critical role in the h_{Ts}. Furthermore, Shao-Horn et al.[36] found that the ORR specific activity of acid leached "Pt_3Co" catalyst can be further increased by annealing it at a high temperature., A so-called "sandwich" structure is formed by driving some of the Co atoms from the core to the subsurface, causing a significant reduction of h_{Ts} from 0.37 to 0.32. This result indicates that the atomic distribution (or alloying extent) also plays an important role in determining h_{Ts}. Similarly, Hwang et al.[84] reported that Pt_1Co_3/C and Pt_1Co_1/C NPs have lower h_{Ts} than Pt/C, whereas Pt_3Co_1/C has higher h_{Ts} than Pt/C and exhibits the poorest activity among the three Pt−Co catalysts. They attributed the decreased h_{Ts} to the charge transfer from Co to Pt, which is promoted by the high Co content as well as the high alloying extent of Pt with Co (J_{Pt}). The charge transfer from Co to Pt within a Pt−Co single-crystal alloy was clearly demonstrated by Hlil et al. using XAS[80] and agrees with the smaller electronegativity of Co (1.88) than that of Pt (2.28). Previously, the activity enhancement of conventional Pt_3M catalysts relative to pure Pt was partly attributed to the increased h_{Ts}.[12,41] However, all of the results above suggest that Pt−Co NPs with high Co content and/or alloying extent present even higher ORR activity despite decreased h_{Ts} that can be safely ascribed to the charge transfer from Co to Pt. This indicates the correlation between the Pt d-band vacancy and the ORR activity of PtM NPs is not straightforward, and thus, its use as a valid descriptor of PtM ORR activity is nontrivial.

The increased Pt $L_{2,3}$ white line intensity at 0.90 V versus 0.54 V (Figure 3b) is understood as the adsorption of oxygenated adsorbates on Pt, which increases the unoccupied d-orbitals of Pt via the charge transfer from Pt to O.[12,13] On the contrary, the Co K edge spectra at 0.54 and 0.90 V are not significantly different. This similarity suggests that most of the metallic Co atoms are protected underneath the surface, otherwise a clear difference caused by the Co oxidation at higher potential would be observed. Thus, these results indicate that both catalysts are composed of Pt-dominated surfaces and Co-rich cores. A more surface-sensitive $\Delta\mu$-XANES analysis reported elsewhere[85] shows that there is some Co in the (near)surface regions of both catalysts under in situ conditions. Therefore, the ligand effects caused by the interactions between surface Pt and subsurface Co cannot be excluded, although it is unclear whether they play an important role in modifying the electronic properties of Pt in the surfaces of PtM NPs as compared to the concomitant strain effects.[26,30,86]

3.3.2. In Situ EXAFS. Previously, we have demonstrated that the ordered face-centered tetragonal (fct) PtCo $L1_0$ structure of D-PtCo/HSC sustains under the environmental conditions of a PEMFC by performing a full single and multiple scattering (SS + MS) analysis of both the Pt L_3 and Co K edge EXAFS data.[87] On the contrary, attempts to fit the D-$PtCo_3$/HSC EXAFS data with SS + MS analysis led to physically unreasonable results. This indicates the lack of long-range order and random substitution of Pt and Co atoms in D-$PtCo_3$/HSC NPs. Thus, it is confirmed that the disordered structure of D-$PtCo_3$/HSC NPs evidenced by the HAADF-STEM imaging (Figure 2) is maintained in acidic operation conditions.

For the purpose of comparison, traditional first shell Fourier Transform (FT) EXAFS analysis was performed on D-$PtCo_3$/HSC and D-PtCo/HSC with similar parameter settings. The fits were applied to Pt L_3 edge and Co K edge concurrently as shown in Figure 4 (the corresponding fit in Re{Chi(R)} and Im{Chi(R)} are displayed in Figure S2 and S3, respectively), and the fitting results are listed in Table 2. Basic constraints were introduced during the fitting:

$$R_{Pt-Co} = R_{Co-Pt} \quad (2)$$

$$\sigma^2_{Pt-Co} = \sigma^2_{Co-Pt} \quad (3)$$

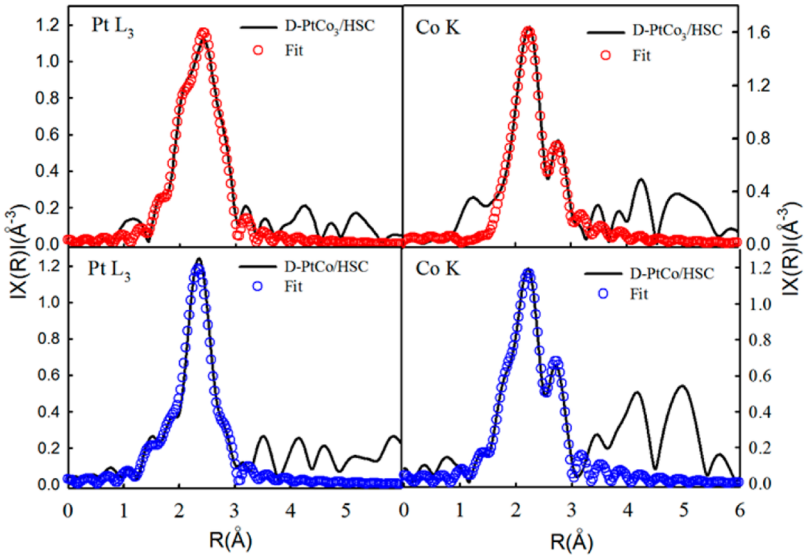

Figure 4. Pt L_3 edge (left) and Co K edge (right) EXAFS spectra (solid black line) collected at 0.54 V in N_2-saturated 0.1 M $HClO_4$ electrolyte and the corresponding first shell least-squares fits (circles) for D-$PtCo_3$/HSC (top) and D-PtCo/HSC (bottom) catalysts. The fits were performed with $k^{1,2,3}$ weighting.

dx.doi.org/10.1021/cs501537n | ACS Catal. 2015, 5, 176−186

Table 2. Summary of EXAFS Results Obtained by Simultaneously Fitting the Pt L_3 and Co K Edge Data for the D-$PtCo_3$/HSC and D-PtCo/HSC in N_2 Sparged 0.1 M $HClO_4$ at 0.54 V[a]

edge	M−M	R	CN	E_0	σ^2	R-factor	J[b]
				D-$PtCo_3$			
Co K	Co−Co	2.58 ± 0.01	5.2 ± 0.5	7.9 ± 0.5	0.007 ± 0.007	0.013	0.96
	Co−Pt	2.63 ± 0.01	6.0 ± 0.7		0.010 ± 0.002		
Pt L_3	Pt−Co	2.63 ± 0.01	2.0 ± 0.7	5.0 ± 0.8	0.010 ± 0.002	0.017	0.71
	Pt−Pt	2.71 ± 0.01	6.3 ± 0.9		0.005 ± 0.001		
				D-PtCo			
Co K	Co−Co	2.65 ± 0.01	3.1 ± 0.4	−3.6 ± 0.5	0.005 ± 0.001	0.010	1.29
	Co−Pt	2.66 ± 0.01	7.4 ± 0.6		0.006 ± 0.006		
Pt L_3	Pt−Co	2.66 ± 0.01	2.9 ± 0.6	6.5 ± 0.9	0.006 ± 0.006	0.017	0.98
	Pt−Pt	2.70 ± 0.01	5.1 ± 0.7		0.004 ± 0.001		

[a] S_0^2 fixed at 0.80 and 0.76 for Pt and Co, respectively, as obtained by fitting the reference foils. Fits were done in R-space, $k^{1,2,3}$ weighting. For Pt, 1.3< R < 3.3 Å and Δk = 2.71−12.26 $Å^{-1}$ were used; for Co, 1.3 < R < 3.06 Å and Δk = 2.539−11.646 $Å^{-1}$ were used. [b] J value derived from the coordination number can be used to quantitatively determine the atomic distribution (or alloying extent) of bimetallic alloys.[61]

Here R_{Pt-Co} (R_{Co-Pt}) is the bond distance for Pt−Co (Co−Pt) scattering, and σ^2_{Pt-Co} (σ^2_{Co-Pt}) are the uncertainties in the bond lengths as suggested by the fitting.

The total coordination number of the Pt, CN_{Pt}, can be calculated as

$$CN_{Pt} = CN_{Pt-Pt} + CN_{Pt-Co} \quad (4)$$

where CN_{Pt-Pt} and CN_{Pt-Co} are the coordination number of Pt−Pt bond and Pt−Co bond, respectively. Similarly,

$$CN_{Co} = CN_{Co-Co} + CN_{Co-Pt} \quad (5)$$

For both catalysts, the CN_{Pt} is smaller than CN_{Co}, which indicates Pt has less metallic neighboring atoms than Co. This result suggests that both catalytic particles have a structure with a Co-rich core and a Pt-dominated surface, where the Pt atoms are under-coordinated, and are in agreement with the aforementioned XANES results. This is expected for dealloyed catalysts, because the dealloying process preferentially dissolves the electrochemically more reactive Co from the $PtCo_x$ precursor, leaving a Pt-rich outer shell.[18]

The average first-shell coordination number of metal−metal neighbors per absorbing atom in D-$PtCo_3$/HSC and D-PtCo/HSC at 0.54 V is determined to be 9.0 and 8.7 from the following equation:

$$CN_{avg} = (n_{Pt/Co}CN_{Pt} + CN_{Co})/(1 + n_{Pt/Co}) \quad (6)$$

where $n_{Pt/Co}$ is the Pt/Co atomic ratio. Because the first-shell coordination number is a strong and nonlinear function of the particle diameter for particles with diameters smaller than 30−50 Å,[88−91] the particle size of the two samples are estimated to be ∼2.5 nm by utilizing Benfield's method and assuming a perfectly solid cuboctahedron morphology.[89] However, the atoms in the (near)surface region of the dealloyed PtM NPs are generally under-coordinated due to the porous surfaces formed during to the dealloying process. In addition, EXAFS usually gives a smaller averaged particle size when compared to XRD and TEM.[92] Therefore, the particle sizes estimated from the CNs are expected to be smaller than those obtained from ADF-STEM (4−5 nm). The averaged CNs of the two catalysts are close, in agreement with their comparable mean particle sizes (Figure 2). In addition, the CN of Pt in D-$PtCo_3$/HSC (8.3 ± 1.6) and D-PtCo/HSC (8.0 ± 1.3) are close, suggesting that its influence on the d-band center will not be significantly different according to eq 1.

The alloying extent or atomic distribution in bimetallic NPs can be determined quantitatively by using J_A and J_B (A and B represent the two elements in bimetallics), with derived structural models based on the alloying extent and coordination number parameters.[61] The extremely high J_{Pt} and J_{Co} values of D-PtCo/HSC indicate a high alloying extent associated with the ordered structure, whereas the relatively lower J_{Pt} and J_{Co} values of D-$PtCo_3$/HSC match the disordered core structure. Furthermore, as the J value of perfectly alloyed bimetallic NPs is equal to 1,[61] the J_{Co} < 1 of D-$PtCo_3$/HSC gives in situ evidence of some degree of local concentration of Co that is directly observed by ex situ HAADF-STEM.

As seen for both D-$PtCo_3$/HSC and D-PtCo/HSC catalysts, the particle morphology of the dry powders obtained by ex situ HAADF STEM is akin to the particle morphology of the in situ electrodes characterized by in situ XAS. This indicates that the bulk structure of the two samples does not change significantly during the early stage of operation. We postulate that this is because the dry powders may have already reached a pseudosteady state during the dealloying process under the harsh and acidic environments.

The R_{Pt-Pt} in D-$PtCo_3$/HSC (2.71 Å) and D-PtCo/HSC (2.70 Å) are much shorter than that in Pt/C (2.75 Å).[45] According to eq 1, the shortening of R_{Pt-Pt} leads to a broadening and negative shift of the Pt d-band as demonstrated previously.[25,93,94] These so-called strain effects have been widely acknowledged as a key determinant to the enhanced ORR activity of PtM catalysts by weakening the Pt−O binding energy and thereby reducing the coverage of surface-blocking species to allow more O_2 to reach the active sites.[12−14] The experimentally determined R_{Pt-Pt} values are extremely close to the theoretical values (2.70 Å for D-$PtCo_3$/HSC and 2.69 Å for D-PtCo/HSC) calculated using the Co/Pt atomic ratio based on Vegard's Law. The similar result was recently reported on dealloyed $PtNi_3$/C NPs.[95] The similar R_{Pt-Pt} between D-$PtCo_3$/HSC and D-PtCo/HSC is attributed to their comparable Pt/Co atomic composition (2.7 vs 2.2). This leads us to conclude that the strain effects in these two samples are also comparable. It is worth mentioning that the bulk average R_{Pt-Pt}(s) of both catalysts are close to the optimal surface Pt−Pt bond distance (∼2.71 Å) in terms of ORR activity proposed by Strasser et al.[25] based on DFT calculations. This might account for the high ORR activities of these two catalysts, although the bulk average R_{Pt-Pt} determined by EXAFS is

dx.doi.org/10.1021/cs501537n | ACS Catal. 2015, 5, 176−186

expected to be shorter than the surface R_{Pt-Pt} owing to the surface relaxation.[25]

The R_{CoCo} in D-PtCo$_3$/HSC (2.58 Å) and D-PtCo/HSC (2.65 Å) are much longer than that in the Co foil, 2.50 Å. Interestingly, these experimental results are very close to the theoretical values (2.57 Å for D-PtCo$_3$/HSC and 2.64 Å for D-PtCo/HSC) calculated using the Co/Pt atomic ratio of the precursors based on Vegard's Law. Thus, it is clear that the Co−Co bond distance is determined by the atomic ratio of the precursor. The R_{PtCo} in D-PtCo/HSC (2.66 Å) is similar to the R_{CoCo} (2.65 Å). This suggests that the majority of the heterometallic interactions in D-PtCo/HSC NPs are located in the Co-rich cores, consistent with the Pt$_{thin\text{-}shell}$/single-PtCo$_{core}$ structure. On the contrary, the R_{PtCo} in D-PtCo$_3$/HSC (2.63 Å) is in between the R_{CoCo} (2.58 Å) and R_{PtPt} (2.71 Å), which suggests that the heterometallic interactions are located in both the Co-rich cores and the Pt-rich surfaces. As the averaged R_{PtCo} in the Pt-rich outer layers is longer than that in the Co-rich cores, it is reasonable to conjecture that the R_{PtCo} in the near(surface) regions of the two catalysts are similar. Consequently, the ligand effects, which are codetermined by the specific element M and the R_{PtM} according to eq 1, shall be comparable between the two catalysts. Moreover, our previous FEFF calculations show that the ligand effects caused by the late 3d elements, such as Co, are negligible when compared to the concurrent strain effects. These similar results were also reported by Nørskov et al.[86] using DFT calculations. This further suggests that the ligand effects in both catalysts are comparable in shifting the d-band center of Pt surfaces.

Overall, despite the different morphology between D-PtCo$_3$/HSC and D-PtCo/HSC NPs, the strain, ligand, and particle size effects are comparable as suggested by their similar R_{PtPt}, R_{PtCo}, and averaged CN of Pt. This gives a plausible explanation on their similar ORR activities.

3.4. Catalytic Performance Degradation of the Dealloyed PtCo$_3$/HSC Catalyst. The catalytic degradation of PtM NPs during long-term operation in PEMFCs is often coimpacted by the interplay of strain, ligand, and particle size effects. Voltage cycling causes not only particle growth,[21,56] but also dissolution of the soluble metal M leading to the attenuation of strain and/or ligand effects.[57] Therefore, EXAFS analysis was applied to aged D-PtCo$_3$/HSC catalyst at different cycling stages to monitor the changes in the bond distance and the coordination number upon cycling, which offers unique insight into the performance degradation as these quantities are directly related of strain, ligand, and particle size effects as aforementioned.

EXAFS data and first-shell fits for the Pt L_3 edge and Co K edge of the D-PtCo$_3$/HSC NPs undergoing different extents of voltage cycling (beginning of life (BOL): ~10 cycles; 10k: 10 000 cycles; and 30k: 30 000 cycles) are displayed in Figure 5. The best-fit values of the structural parameters are summarized in Table 3. The leaching of Co is clearly seen on the left side of Figure 5, which shows that the contribution of Pt−Pt scattering (identified as the gray line) over the whole scattering peak increases with increasing voltage cycles. Correspondingly, the surrounding numbers of Co atom seen by Pt, CN_{Pt-Co}, continuously reduces. After 30k cycles, the Pt−Pt scattering almost dominates the total scattering peak, indicating only a trivial amount of Co remained in the catalyst. The extremely similar FT peaks between the 30k catalyst and the corresponding Pt reference foil (multiplied by a factor of 0.75 for comparison) indicates that the 30k D-PtCo$_3$/HSC has a Pt-like structure, which is further supported by the R_{PtPt} (2.75 Å) that is equal to that of pure Pt/C NPs. The formation of a Pt-like structure is partly ascribed to the Co leaching from the NPs. Moreover, it has long been known that the Pt in PtM catalysts can be dissolved upon long-term fuel cell operation as well, and the dissolved Pt ions can redeposit onto larger NPs (Ostwald ripening), and/or diffuse toward the cathode/membrane interface and form large Pt crystallites in the ionomer phase.[57,96−98] Because the cathode electrode together with the membrane were placed in the path of the X-ray in this work, the EXAFS results are averaged over all the Pt atoms in the catalyst, the ionomer of the electrode, and the membrane owing to the bulk-averaged nature of XAS technique. Therefore, the Pt-like structure identified here cannot be exclusively assigned to the 30k D-PtCo$_3$/HSC catalyst in the electrode. Because of this interference, in situ XAS was not conducted on these catalysts.

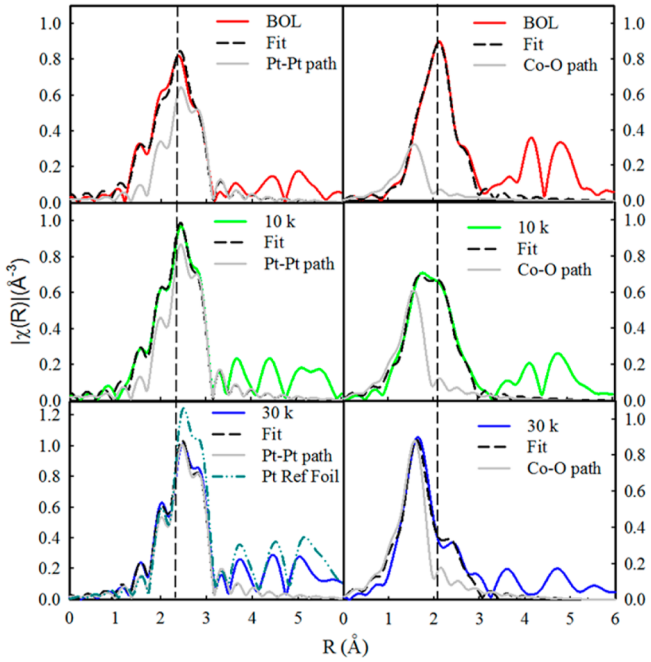

Figure 5. Pt L_3 edge (left) and Co K edge (right) EXAFS spectra and the corresponding least-squares fits for D-PtCo$_3$/HSC catalyst under different voltage cycling stages: BOL (top), 10k (middle), and 30k (bottom).

The interference between the XAS signal coming from the Co in the membrane/ionomer and in the electrode is even more apparent. As shown on the right side of Figure 5, the contribution of Co−O scattering increases with increased voltage cycling, associated with the increase of CN_{Co-O} (Table 3). Because the Co oxides cannot survive in the acidic and oxidizing environment of a PEMFC cathode, these results indicate that dissolved Co during voltage cycling electromigrates into the membrane and forms Co oxides, which results in the decrease of the local proton concentration (proton starvation) and hereby reduces the performance of the fuel cell, especially at high current density.[99]

The gradual increase in Pt−Pt bond length from 2.71 to2.75 Å with Co loss clearly demonstrates the attenuation of strain effects during voltage cycling. In addition, the 30k D-PtCo$_3$/HSC catalyst suffering nearly complete loss of Co must not have substantial Co atoms in subsurface causing the ligand effects to be entirely eliminated considering their limited

dx.doi.org/10.1021/cs501537n | ACS Catal. 2015, 5, 176−186

Table 3. Summary of Ex Situ EXAFS Results of Aged D-PtCo$_3$/HSC[a]

edge	scattering	R (ΔR = ± 0.01 Å)[b]	CN (ΔN = ± 0.7)[b]	σ^2 ($\Delta\sigma^2$= ± 0.007 Å^2)[b]	E_0 (ΔE_0 = 1.5 eV)[b]
BOL					
Pt L_3	Pt−Pt	2.71	5.2	0.006	7.3
	Pt−Co	2.63	2.2	0.012	7.3
	Pt−O	1.98	0.8	0.005	7.3
Co K	Co−Co	2.59	3.9	0.011	−5.1
	Co−Pt	2.63	6.4	0.012	−5.1
	Co−O	2.05	1.5	0.005	−5.1
10 k					
Pt L_3	Pt−Pt	2.73	7.0	0.006	7.3
	Pt−Co	2.64	1.5	0.012	7.3
	Pt−O	1.98	0.6	0.005	7.3
Co K	Co−Co	2.59	3.1	0.011	−5.1
	Co−Pt	2.64	5.6	0.012	−5.1
	Co−O	2.05	2.9	0.005	−5.1
30 k					
Pt L_3	Pt−Pt	2.75	8.3	0.006	7.3
	Pt−Co	2.66	0.6	0.012	7.3
	Pt−O	1.98	0.3	0.005	7.3
Co K	Co−Co	2.59	1.7	0.011	−5.1
	Co−Pt	2.66	4.4	0.012	−5.1
	Co−O	2.05	4.2	0.005	−5.1

[a]S_0^2 fixed at 0.80 and 0.76 for Pt and Co, respectively, as obtained by fitting the reference foils. Fits were done in R-space, $k^{1,2,3}$ weighting. For Pt, 1.1 < R < 3.2 Å and Δk = 3.08−12.22 Å^{-1} were used; for Co, 1.05< R < 3 Å and Δk = 2.73−11.09 Å^{-1} were used. [b]Values represent the largest statistical errors of all of the least-squares fits determined by ARTEMIS.

effective range.[100] The particle size effect cannot be evaluated based on the CN determined by ex situ EXAFS, because it can significantly deviate from the CN of the catalyst in the in situ electrode due to the interference. However, the drop of the ECSAs (Figure 1) for this catalyst strongly suggests that the particle size growth and/or the smoothening of the Pt corners and edges occurs during voltage cycling lead to the removal of under-coordinated Pt atoms. Thus, the SA governed by the particle size effects is expected to increase with voltage cycling, which has been clearly demonstrated in the aforementioned pure Pt/C NPs in voltage-cycled electrodes.[2,56,101] The ECSA loss of D-PtCo/HSC and D-PtCo$_3$/HSC (~30%) during voltage cycling is significantly less when compared to Pt/C (~75%[21,56]), which is well understood as the high-temperature annealing process (900 °C here) that results in larger, more stable NPs similar to the behavior of high temperature annealed pure Pt/C NPs.[56]

Because the strain and ligand effects in the 30k D-PtCo$_3$/HSC with a Pt-like structure are negligible, the SA is predominately determined by the particle size effects. This is further supported by the final SA of 30k D-PtCo$_3$/HSC (1030 μA·cm$^2_{Pt}$) which lies in the range reported for pure Pt/C NPs undergoing 30k voltage cycles from 0.5 to 1.0 V in PEMFCs (30 wt % Pt/HSC: 787 μA·cm$^2_{Pt}$; 45 wt % Pt/Vu: 1056 μA·cm$^2_{Pt}$).[21] On the other hand, the initial SA of fresh D-PtCo$_3$/HSC (1000 μA·cm$^2_{Pt}$) is most likely codetermined by all the three effects, and happens to be close to that of the 30k D-PtCo$_3$/HSC catalyst. As a result, the SA of D-PtCo$_3$/HSC catalyst remains constant within the 30k voltage cycles in PEMFCs. The constant SA with voltage cycling has been previously reported on Pt−Co/C NPs tested in PEMFCs under various conditions.[53−55] Although it is tempting to attribute the stable SA of D-PtCo$_3$/HSC and D-PtCo/HSC with voltage cycling to the counterbalance between strain, ligand, and particle size effects associated with the particle morphology transformation, in situ experimental data on the atomic-scale structure of PtM NPs at different voltage cycling stages is required to fully understand the SA trend with voltage cycling. An ongoing study using in situ XAS on dealloyed PtM NP catalysts coated on diffusion media (CCDMs), which allow catalysts to be detached from MEA assemblies before being transferred into an electrochemical XAS half cell, will aim to avoid the interference.

4. CONCLUSION

In summary, we reported that the D-PtCo/HSC and D-PtCo$_3$/HSC catalysts exhibit the same levels of enhancement in ORR activity and durability over Pt/C NPs despite that they possess distinctly different initial Co content and bulk morphology: D-PtCo/HSC is dominated by nanoparticles with Pt shells surrounding a single ordered PtCo core, while D-PtCo$_3$/HSC is dominated by nanoparticles with Pt shells surrounding multiple disordered PtCo cores with local concentration of Co. In situ XAS further confirms that their bulk morphologies are retained under the electrochemical acidic environment during reactions. Advanced in situ XAS analysis was conducted to reveal the structural origin of their enhanced ORR performance at the fundamental level. We showed that these two catalysts possess similar Pt−Pt and Pt−Co bond distances and Pt coordination numbers (CNs) albeit their dissimilar morphologies, and the similar activity is thus ascribed to the comparable strain, ligand, and particle size effects. Ex situ XAS performed on dealloyed PtCo$_3$/HSC at different voltage cycling stages showed the continuous dissolution of Co, leaving behind NPs with a Pt-like structure containing only a trivial amount of Co after 30k cycles. The resultant attenuation in strain and/or ligand effects are presumably counterbalanced by the particle size effects, which is proposed to account for the constant specific activity with voltage cycling.

dx.doi.org/10.1021/cs501537n | ACS Catal. 2015, 5, 176−186

■ ASSOCIATED CONTENT

Supporting Information

The following file is available free of charge on the ACS Publications website at DOI: 10.1021/cs501537n.

Additional information including the raw XAS spectra at the Pt L_3 and Co K edges in k space, the EXAFS fitting results in real and imaginary R space are provided in a supporting file (PDF)

■ AUTHOR INFORMATION

Corresponding Author

*E-mail: s.mukerjee@neu.edu. Phone: (617)373-2382.

Notes

The authors declare no competing financial interest.

■ ACKNOWLEDGMENTS

This research was supported by the Fuel Cell Technology Program of the Office of Energy Efficiency and Renewable Energy of the U.S. Department of Energy under contract DE-EE0000458. Use of the Advanced Photon Source (beamline XOR-9BM), Argonne National Laboratory and the National Synchrotron Light Source (beamline X3B), Brookhaven National Laboratory was supported by the U.S. Department of Energy, Office of Science, Office of Basic Energy Sciences, under Contract No. DE-AC02-98CH10886. This publication was made possible by the Center for Synchrotron Biosciences grant, P30-EB-009998, from the National Institute of Biomedical Imaging and Bioengineering (NBIB). Support from beamline personnel Dr. Erik Farquhar and Mark Chance (X3B) is gratefully acknowledged.

■ REFERENCES

(1) Wagner, F. T.; Lakshmanan, B.; Mathias, M. F. *J. Phys. Chem. Lett.* **2010**, *1*, 2204−2219.
(2) Gasteiger, H. A.; Kocha, S. S.; Sompalli, B.; Wagner, F. T. *Appl. Catal., B* **2005**, *56*, 9−35.
(3) Wang, Y.; Chen, K. S.; Mishler, J.; Cho, S. C.; Adroher, X. C. *Appl. Energ* **2011**, *88*, 981−1007.
(4) Lefèvre, M.; Proietti, E.; Jaouen, F.; Dodelet, J.-P. *Science* **2009**, *324*, 71−74.
(5) Beard, B. C.; Philip, N.; Ross, J. *J. Electrochem. Soc.* **1990**, *137*, 3368−3374.
(6) Paulus, U. A.; Wokaun, A.; Scherer, G. G.; Schmidt, T. J.; Stamenkovic, V.; Radmilovic, V.; Markovic, N. M.; Ross, P. N. *J. Phys. Chem. B* **2002**, *106*, 4181−4191.
(7) Soderberg, J. N.; Sirk, A. H. C.; Campbell, S. A.; Birss, V. I. *J. Electrochem. Soc.* **2005**, *152*, A2017−A2022.
(8) Paulus, U. A.; Wokaun, A.; Scherer, G. G.; Schmidt, T. J.; Stamenkovic, V.; Markovic, N. M.; Ross, P. N. *Electrochim. Acta* **2002**, *47*, 3787−3798.
(9) Lima, F. H. B.; Giz, M. J.; Ticianelli, E. A. *J. Braz. Chem. Soc.* **2005**, *16*, 328−336.
(10) Antolini, E.; Salgado, J. R. C.; Giz, M. J.; Gonzalez, E. R. *Int. J. Hydrogen Energy* **2005**, *30*, 1213−1220.
(11) Min, M.-k.; Cho, J.; Cho, K.; Kim, H. *Electrochim. Acta* **2000**, *45*, 4211−4217.
(12) Mukerjee, S.; Srinivasan, S. *J. Electroanal. Chem.* **1993**, *357*, 201−224.
(13) Mukerjee, S.; Srinivasan, S.; Soriaga, M. P.; McBreen, J. *J. Phys. Chem.* **1995**, *99*, 4577−4589.
(14) Mukerjee, S.; Srinivasan, S.; Soriaga, M. P.; McBreen, J. *J. Electrochem. Soc.* **1995**, *142*, 1409−1422.
(15) Stamenković, V.; Schmidt, T. J.; Ross, P. N.; Marković, N. M. *J. Phys. Chem. B* **2002**, *106*, 11970−11979.
(16) Stamenkovic, V.; Mun, B. S.; Mayrhofer, K. J. J.; Ross, P. N.; Markovic, N. M.; Rossmeisl, J.; Greeley, J.; Nørskov, J. K. *Angew. Chem., Int. Ed.* **2006**, *45*, 2897−2901.
(17) Xiong, L.; Manthiram, A. *J. Electrochem. Soc.* **2005**, *152*, A697−A703.
(18) Koh, S.; Strasser, P. *J. Am. Chem. Soc.* **2007**, *129*, 12624−12625.
(19) Oezaslan, M.; Strasser, P. *J. Power Sources* **2011**, *196*, 5240−5249.
(20) Hasché, F.; Oezaslan, M.; Strasser, P. *J. Electrochem. Soc.* **2012**, *159*, B24−B33.
(21) Neyerlin, K. C.; Srivastava, R.; Yu, C.; Strasser, P. *J. Power Sources* **2009**, *186*, 261−267.
(22) GreeleyJ; Stephens, I. E. L.; Bondarenko, A. S.; Johansson, T. P.; Hansen, H. A.; Jaramillo, T. F.; RossmeislJ; ChorkendorffI; Nørskov, J. K. *Nat. Chem.* **2009**, *1*, 552−556.
(23) Hammer, B.; Nørskov, J. K. In *Advances in Catalysis*; Bruce, C. Gates, H. K., Ed.; Academic Press: San Diego, CA, 2000; Vol. *45*, pp 71−129.
(24) Stamenkovic, V. R.; Mun, B. S.; Arenz, M.; Mayrhofer, K. J. J.; Lucas, C. A.; Wang, G.; Ross, P. N.; Markovic, N. M. *Nat. Mater.* **2007**, *6*, 241−247.
(25) Strasser, P.; Koh, S.; Anniyev, T.; Greeley, J.; More, K.; Yu, C.; Liu, Z.; Kaya, S.; Nordlund, D.; Ogasawara, H.; Toney, M. F.; Nilsson, A. *Nat. Chem.* **2010**, *2*, 454−460.
(26) Jia, Q.; Segre, C. U.; Ramaker, D.; Caldwell, K.; Trahan, M.; Mukerjee, S. *Electrochim. Acta* **2013**, *88*, 604−613.
(27) Stamenkovic, V. R.; Mun, B. S.; Mayrhofer, K. J. J.; Ross, P. N.; Markovic, N. M. *J. Am. Chem. Soc.* **2006**, *128*, 8813−8819.
(28) Wang, J. X.; Inada, H.; Wu, L.; Zhu, Y.; Choi, Y.; Liu, P.; Zhou, W.-P.; Adzic, R. R. *J. Am. Chem. Soc.* **2009**, *131*, 17298−17302.
(29) Stamenkovic, V. R.; Fowler, B.; Mun, B. S.; Wang, G.; Ross, P. N.; Lucas, C. A.; Marković, N. M. *Science* **2007**, *315*, 493−497.
(30) Kitchin, J. R.; Nørskov, J. K.; Barteau, M. A.; Chen, J. G. *J. Chem. Phys.* **2004**, *120*, 10240−10246.
(31) Hammer, B.; Norskov, J. K. *Nature* **1995**, *376*, 238−240.
(32) Mun, B. S.; Watanabe, M.; Rossi, M.; Stamenkovic, V.; Markovic, N. M.; Philip, N.; Ross, J. *J. Chem. Phys.* **2005**, *123*, 204717.
(33) Rabis, A.; Rodriguez, P.; Schmidt, T. J. *ACS Catal.* **2012**, *2*, 864−890.
(34) Stephens, I. E. L.; Bondarenko, A. S.; Gronbjerg, U.; Rossmeisl, J.; Chorkendorff, I. *Energ Environ. Sci.* **2012**, *5*, 6744−6762.
(35) Yu, T. H.; Hofmann, T.; Sha, Y.; Merinov, B. V.; Myers, D. J.; Heske, C.; Goddard, W. A. *J. Phys. Chem. C* **2013**, *117*, 26598−26607.
(36) Chen, S.; Sheng, W.; Yabuuchi, N.; Ferreira, P. J.; Allard, L. F.; Shao-Horn, Y. *J. Phys. Chem. C* **2008**, *113*, 1109−1125.
(37) Tuaev, X.; Rudi, S.; Petkov, V.; Hoell, A.; Strasser, P. *ACS Nano* **2013**, *7*, 5666−5674.
(38) Cui, C.; Gan, L.; Heggen, M.; Rudi, S.; Strasser, P. *Nat. Mater.* **2013**, *12*, 765−771.
(39) Wang, C.; Chi, M.; Li, D.; Strmcnik, D.; van der Vliet, D.; Wang, G.; Komanicky, V.; Chang, K.-C.; Paulikas, A. P.; Tripkovic, D.; Pearson, J.; More, K. L.; Markovic, N. M.; Stamenkovic, V. R. *J. Am. Chem. Soc.* **2011**, *133*, 14396−14403.
(40) Kitchin, J. R.; Nørskov, J. K.; Barteau, M. A.; Chen, J. G. *Phys. Rev. Lett.* **2004**, *93*, 156801.
(41) Toda, T.; Igarashi, H.; Uchida, H.; Watanabe, M. *J. Electrochem. Soc.* **1999**, *146*, 3750−3756.
(42) Xin, H. L.; Mundy, J. A.; Liu, Z.; Cabezas, R.; Hovden, R.; Kourkoutis, L. F.; Zhang, J.; Subramanian, N. P.; Makharia, R.; Wagner, F. T.; Muller, D. A. *Nano Lett.* **2011**, *12*, 490−497.
(43) Wang, D.; Xin, H. L.; Hovden, R.; Wang, H.; Yu, Y.; Muller, D. A.; DiSalvo, F. J.; Abruña, H. D. *Nat. Mater.* **2013**, *12*, 81−87.
(44) Shao, M.; Peles, A.; Shoemaker, K. *Nano Lett.* **2011**, *11*, 3714−3719.
(45) Mukerjee, S.; McBreen, J. *J. Electroanal. Chem.* **1998**, *448*, 163−171.
(46) Kinoshita, K. *J. Electrochem. Soc.* **1990**, *137*, 845−848.

(47) Nesselberger, M.; Ashton, S.; Meier, J. C.; Katsounaros, I.; Mayrhofer, K. J. J.; Arenz, M. *J. Am. Chem. Soc.* **2011**, *133*, 17428−17433.
(48) Sheng, W.; Chen, S.; Vescovo, E.; Shao-Horn, Y. *J. Electrochem. Soc.* **2011**, *159*, B96−B103.
(49) Mayrhofer, K. J. J.; Strmcnik, D.; Blizanac, B. B.; Stamenkovic, V.; Arenz, M.; Markovic, N. M. *Electrochim. Acta* **2008**, *53*, 3181−3188.
(50) Hammer, B.; Nielsen, O. H.; Nrskov, J. K. *Catal. Lett.* **1997**, *46*, 31−35.
(51) Hvolbæk, B.; Janssens, T. V. W.; Clausen, B. S.; Falsig, H.; Christensen, C. H.; Nørskov, J. K. *Nano Today* **2007**, *2*, 14−18.
(52) Han, B. C.; Miranda, C. R.; Ceder, G. *Phys. Rev. B* **2008**, *77*, 075410.
(53) Yu, P.; Pemberton, M.; Plasse, P. *J. Power Sources* **2005**, *144*, 11−20.
(54) Ball, S. C.; Theobald, B.; Thompsett, D.; Hudson, S. *ECS Trans* **2006**, *1*, 141−152.
(55) Wagner, F. T.; Gasteiger, H. A.; Makharia, R.; Neyerlin, K. C.; Thompson, E. L.; Yan, S. G. *ECS Trans* **2006**, *3*, 19−29.
(56) Makharia, R.; Kocha, S.; Yu, P.; Sweikart, M. A.; Gu, W.; Wagner, F.; Gasteiger, H. A. *ECS Trans* **2006**, *1*, 3−18.
(57) Chen, S.; Gasteiger, H. A.; Hayakawa, K.; Tada, T.; Shao-Horn, Y. *J. Electrochem. Soc.* **2010**, *157*, A82−A97.
(58) Debe, M. K.; Schmoeckel, A. K.; Vernstrom, G. D.; Atanasoski, R. *J. Power Sources* **2006**, *161*, 1002−1011.
(59) Teliska, M.; Murthi, V. S.; Mukerjee, S.; Ramaker, D. E. *J. Electrochem. Soc.* **2005**, *152*, A2159−A2169.
(60) Zhang, J.; Vukmirovic, M. B.; Sasaki, K.; Nilekar, A. U.; Mavrikakis, M.; Adzic, R. R. *J. Am. Chem. Soc.* **2005**, *127*, 12480−12481.
(61) Hwang, B.-J.; Sarma, L. S.; Chen, J.-M.; Chen, C.-H.; Shih, S.-C.; Wang, G.-R.; Liu, D.-G.; Lee, J.-F.; Tang, M.-T. *J. Am. Chem. Soc.* **2005**, *127*, 11140−11145.
(62) Teliska, M.; O'Grady, W. E.; Ramaker, D. E. *J. Phys. Chem. B* **2004**, *108*, 2333−2344.
(63) Roth, C.; Benker, N.; Buhrmester, T.; Mazurek, M.; Loster, M.; Fuess, H.; Koningsberger, D. C.; Ramaker, D. E. *J. Am. Chem. Soc.* **2005**, *127*, 14607−14615.
(64) Jia, Q.; Ramaker, D. E.; Ziegelbauer, J. M.; Ramaswamy, N.; Halder, A.; Mukerjee, S. *J. Phys. Chem. C* **2013**, *117*, 4585−4596.
(65) Teliska, M.; Murthi, V. S.; Mukerjee, S.; Ramaker, D. E. *J. Phys. Chem. C* **2007**, *111*, 9267−9274.
(66) Mani, P.; Srivastava, R.; Strasser, P. *J. Phys. Chem. C* **2008**, *112*, 2770−2778.
(67) Koh, S.; Hahn, N.; Yu, C.; Strasser, P. *J. Electrochem. Soc.* **2008**, *155*, B1281−B1288.
(68) Newville, M. *J. Synchrotron Radiat* **2001**, *8*, 322−324.
(69) Ravel, B.; Gallagher, K. *Phys. Scr.* **2005**, *2005*, 606.
(70) Newville, M.; Limacrvincedilscaron, P.; Yacoby, Y.; Rehr, J. J.; Stern, E. A. *Phys. Rev. B* **1993**, *47*, 14126.
(71) Ankudinov, A. L.; Ravel, B.; Rehr, J. J.; Conradson, S. D. *Phys. Rev. B* **1998**, *58*, 7565−7576.
(72) DOE *Hydrogen and Fuel Cell Activities, Progress, and Plans*; Report to Congress. United States Department of Energy: Washington, DC, 2009.
(73) Wagner, F. T. *High-Activity Dealloyed Catalysts. 2012 Annual Merit Review Proceedings - Fuel Cells* [Online Early Access]. Published Online: 2012. http://www.hydrogen.energy.gov/annual_review12_fuelcells.html (accessed October 7, 2012).
(74) Chen, S.; Ferreira, P. J.; Sheng, W.; Yabuuchi, N.; Allard, L. F.; Shao-Horn, Y. *J. Am. Chem. Soc.* **2008**, *130*, 13818−13819.
(75) Yu, Z.; Zhang, J.; Liu, Z.; Ziegelbauer, J. M.; Xin, H.; Dutta, I.; Muller, D. A.; Wagner, F. T. *J. Phys. Chem. C* **2012**, *116*, 19877−19885.
(76) Liu, Z.; Xin, H.; Yu, Z.; Zhu, Y.; Zhang, J.; Mundy, J. A.; Muller, D. A.; Wagner, F. T. *J. Electrochem. Soc.* **2012**, *159*, F554−F559.
(77) Erlebacher, J.; Aziz, M. J.; Karma, A.; Dimitrov, N.; Sieradzki, K. *Nature* **2001**, *410*, 450−453.
(78) Watanabe, M.; Tsurumi, K.; Mizukami, T.; Nakamura, T.; Stonehart, P. *J. Electrochem. Soc.* **1994**, *141*, 2659−2668.
(79) Leroux, C.; Cadeville, M. C.; Pierron-Bohnes, V.; Inden, G.; Hinz, F. *J. Phys. F: Met. Phys.* **1988**, *18*, 2033 DOI: 10.1088/0305-4608/18/9/021.
(80) Hlil, E. K.; Baudoing-Savois, R.; Moraweck, B.; Renouprez, A. J. *J. Phys. Chem.* **1996**, *100*, 3102−3107.
(81) Wang, X.; Li, N.; Pfefferle, L. D.; Haller, G. L. *Catal. Today* **2009**, *146*, 160−165.
(82) Moraweck, B.; Renouprez, A. J.; Hlil, E. K.; Baudoing-Savois, R. *J. Phys. Chem.* **1993**, *97*, 4288−4292.
(83) Mansour, A. N.; Cook, J. W.; Sayers, D. E. *J. Phys. Chem.* **1984**, *88*, 2330−2334.
(84) Lai, F.-J.; Sarma, L. S.; Chou, H.-L.; Liu, D.-G.; Hsieh, C.-A.; Lee, J.-F.; Hwang, B.-J. *J. Phys. Chem. C* **2009**, *113*, 12674−12681.
(85) Kongkanand, A.; Wagner, F., 2014 *Annual Merit Review, US Department of Energy Hydrogen and Fuel Cells Program*, accessed July 30, 2014 http://www.hydrogen.energy.gov/pdfs/review14/fc087_kongkanand_2014_o.pdf.
(86) Ruban, A.; Hammer, B.; Stoltze, P.; Skriver, H. L.; Nørskov, J. K. *J. Mol. Catal. A: Chem.* **1997**, *115*, 421−429.
(87) Jia, Q.; Caldwell, K.; Ramaker, D. E.; Ziegelbauer, J. M.; Liu, Z.; Yu, Z.; Trahan, M.; Mukerjee, S. *J. Phys. Chem. C* **2014**, *118*, 20496−20503.
(88) Arruda, T. M.; Shyam, B.; Ziegelbauer, J. M.; Mukerjee, S.; Ramaker, D. E. *J. Phys. Chem. C* **2008**, *112*, 18087−18097.
(89) Benfield, R. E. *J. Chem. Soc., Faraday Trans.* **1992**, *88*, 1107−1110.
(90) Via, G. H.; Sinfelt, J. H.; Lytle, F. W. *J. Chem. Phys.* **1979**, *71*, 690.
(91) Greegor, R. B.; Lytle, F. W. *J. Catal.* **1980**, *36*, 476−486.
(92) Ashcroft, A. T.; Cheetham, A. K.; Harris, P. J. F.; Jones, R. H.; Natarajan, S.; Sankar, G.; Stedman, N. J.; Thomas, J. M. *Catal. Lett.* **1994**, *24*, 47−57.
(93) Xu, Y.; Ruban, A. V.; Mavrikakis, M. *J. Am. Chem. Soc.* **2004**, *126*, 4717−4725.
(94) Mavrikakis, M.; Hammer, B.; oslash; rskov, J. K. *Phys. Rev. Lett.* **1998**, *81*, 2819.
(95) Jia, Q.; Caldwell, K.; Ziegelbauer, J. M.; Kongkanand, A.; Wagner, F. T.; Mukerjee, S.; Ramaker, D. E. *J. Electrochem. Soc.* **2014**, *161*, F1323−F1329.
(96) Ferreira, P. J.; la O', G. J.; Shao-Horn, Y.; Morgan, D.; Makharia, R.; Kocha, S.; Gasteiger, H. A. *J. Electrochem. Soc.* **2005**, *152*, A2256−A2271.
(97) Akita, T.; Taniguchi, A.; Maekawa, J.; Siroma, Z.; Tanaka, K.; Kohyama, M.; Yasuda, K. *J. Power Sources* **2006**, *159*, 461−467.
(98) Yasuda, K.; Taniguchi, A.; Akita, T.; Ioroi, T.; Siroma, Z. *J. Electrochem. Soc.* **2006**, *153*, A1599−A1603.
(99) Greszler, T. A.; Moylan, T. E.; Gasteiger, H. A. *Handbook of Fuel Cells*; John Wiley & Sons, Ltd: New York, 2010.
(100) Schlapka, A.; Lischka, M.; Gro; szlig, A.; auml; sberger, U.; Jakob, P. *Phys. Rev. Lett.* **2003**, *91*, 016101.
(101) Shao-Horn, Y.; Sheng, W. C.; Chen, S.; Ferreira, P. J.; Holby, E. F.; Morgan, D. *Top. Catal.* **2007**, *46*, 285−305.